PHYSICAL REVIEW X **13,** 031039 (2023)

Imaging with an Ultrathin Reciprocal Lens

Wenzhe Liu,[1,*] Jingguang Chen,[2] Tongyu Li,[2] Zhe Zhang,[2] Fang Guan,[2] Lei Shi,[2] Jian Zi,[2,†] and C. T. Chan[1,‡]
[1]*Department of Physics, The Hong Kong University of Science and Technology, Hong Kong 999077, China*
[2]*State Key Laboratory of Surface Physics, Key Laboratory of Micro- and Nano-Photonic Structures (Ministry of Education), and Department of Physics, Fudan University, Shanghai 200433, China*

(Received 16 November 2022; revised 9 August 2023; accepted 23 August 2023; published 29 September 2023)

Imaging is of great importance in everyday life and various fields of science and technology. Conventional imaging is achieved by bending light rays originating from an object with a lens. Such ray bending requires space-variant structures, inevitably introducing a geometric center to the lens. To overcome the limitations arising from the conventional imaging mechanism, we consider imaging elements that employ a different mechanism, which we call reciprocal lenses. This type of imaging element relies on lateral ray shifting, enabled by momentum-space-variant phase modulations in periodic structures. As such, it has the distinct advantage of not requiring alignment with a geometric center. Moreover, upright real images can be produced directly with a single reciprocal lens as the directions of rays are not changed. We realize an ultrathin reciprocal lens based on a photonic crystal slab. We characterize the lateral ray shifting behavior of the reciprocal lens and demonstrate imaging. Our work gives an alternative mechanism for imaging and provides a new way to modulate electromagnetic waves.

DOI: 10.1103/PhysRevX.13.031039 Subject Areas: Metamaterials, Optics, Photonics

I. INTRODUCTION

Lenses have played a fundamental role in imaging since they were first introduced. They are essential in producing images and enabling us to see objects ranging from bacteria to distant stars [1–3]. While lenses made from biological light-bending structures have evolved in animal species from every major phylum, artificial lenses have revolutionized almost every field of science and technology, from semiconductor device fabrication [4,5] to observation of the cosmos [6,7]. In the past decade, a new type of lens called "metalenses" has been developed. Unlike conventional lenses which are bulky, metalenses use subwavelength resonators to modulate electromagnetic waves [8–17]. However, like conventional lenses, metalenses have limitations due to their need for precise alignment to produce high-quality images. In addition, a single lens will obey the Gaussian lens formula and can only produce inverted real images, requiring a system of lenses to obtain upright real images. In this work, we introduce another class of lenses, called "reciprocal lenses," which follow a distinct lens formula and have a different imaging mechanism. A single reciprocal lens has no geometric center and can produce upright real images. Our experimental realization of an ultrathin reciprocal lens in the microwave range not only verifies the imaging mechanism of reciprocal lenses but also demonstrates the potential for practical applications.

II. REVISITING CONVENTIONAL LENSES

We first revisit the concept and imaging mechanism of conventional lenses before we introduce the notion of "reciprocal lenses." Only the far-field propagation of waves will be considered, and we take the viewpoint of ray optics for ease of understanding. In a nutshell, an ideal lens focuses electromagnetic waves by bending rays differently at different positions in the lens plane, as illustrated in Fig. 1. The lens is assumed to be cylindrically symmetric about the z axis for simplicity, and we reduce the system to a two-dimensional problem in the x-z plane for now. For each ray intersecting the lens plane at x, the angle of propagation would change by $\Delta\theta(x)$. In the paraxial limit, the angle change $\Delta\theta(x)$ equals $-\Delta k_x(x)/k_0$, where Δk_x is the change in the projected wave vector of the ray in the lens plane and k_0 is the free-space wave vector. The lens can focus rays emitted from a point source to another point, following the Gaussian lens formula $1/u + 1/v = \Delta\theta(x)/x = 1/f$ (u, v: the distances from the object and the image to the lens in the z direction; f: the focal length of the lens) [1–3]. Therefore, we obtain

$$\Delta k_x(x) = -k_0 x/f. \tag{1}$$

---

[*] wliubh@connect.ust.hk
[†] jzi@fudan.edu.cn
[‡] phchan@ust.hk

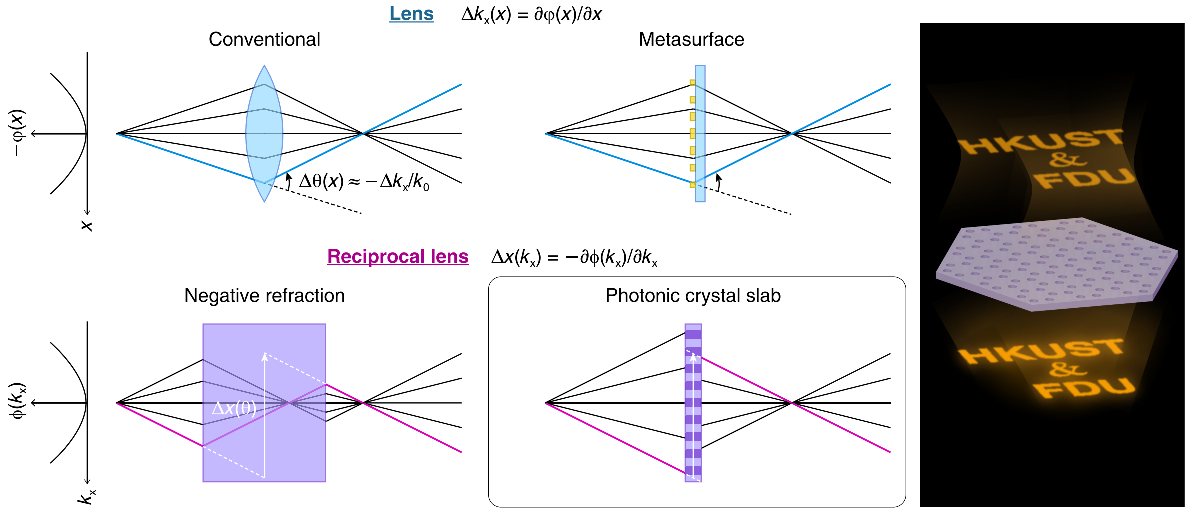

FIG. 1. Schematics of the proposed imaging mechanism compared to existing mechanisms. From the viewpoint of ray optics, imaging is realized by bending rays at different positions. Conventional lenses bend rays by refraction using a curved high-refractive index medium. Metalenses bend rays by using metasurfaces carrying subwavelength resonators and are thinner than conventional lenses. All these lenses produce inverted real images. There is another class of lenses, which we call "reciprocal lens." Instead of bending rays, they produce images by angle-dependent shifting of rays, as illustrated. Bulky reciprocal lenses can be realized in theory based on negative refraction. Here, we report our experimental realization of an ultrathin reciprocal lens by implementing a photonic crystal slab. One particular ray for each mechanism has been highlighted to show the difference. As shown, the image produced by our reciprocal lens is upright but real.

Such a change in the wave vector can arise from a space-variant extra phase $\varphi(x)$ passing through the lens plane. The gradient of the phase change $\partial\varphi(x)/\partial x$ determines the wave vector change [18,19]; thus, we have

$$\Delta k_x(x) = \partial\varphi(x)/\partial x = -k_0 x/f,$$
$$\varphi(x) = -\frac{k_0 x^2}{2f} + \text{const.} \tag{2}$$

The constant can be neglected here. In other words, any optical element with a phase profile $\varphi(x) = -k_0 x^2/2f$ can function as a lens [3,19] because it can focus rays and images in the paraxial limit. A conventional lens introduces the phase profile by refraction through a bulk material. Alternatively, the required phase profile can be realized by specific space-variant resonances in a thin metalens.

III. RECIPROCAL LENSES: IMAGING ELEMENTS BASED ON RAY SHIFTING

After reviewing the focusing and imaging mechanism of lenses, an interesting question arises: Can electromagnetic waves be focused to produce images without bending rays? The answer is affirmative, as focusing and imaging can be realized by ray shifting. If each ray emitted by a point source can be shifted in the z direction by an identical distance $\tilde{f}$ after passing through some structure, an image of the source will be produced.

Rays are straight lines that have no distinct starting or ending points. While it is difficult to find a structure that can shift rays in the z axis, a ray with an incident angle θ can be shifted in the x axis by a distance Δx to produce an identical effect. In the paraxial limit, it will be $\Delta x(\theta) = \tilde{f} \cdot \theta$. Since we have $k_x \approx -k_0\theta$, we can express Δx with the in-plane wave vector k_x:

$$\Delta x(k_x) = -\tilde{f} k_x/k_0. \tag{3}$$

The shifts of rays result from the extra phase gradient in the wave-vector space (momentum space) passing through the structure [20]; therefore, we have

$$\frac{\partial\phi(k_x)}{\partial k_x} = -\Delta x(k_x) = \tilde{f} k_x/k_0,$$
$$\phi(k_x) = \frac{\tilde{f} k_x^2}{2k_0} + \text{const.} \tag{4}$$

We can conclude that any structure that provides an isotropic quadratic momentum-space phase modulation $\phi(\mathbf{k}_\parallel) \sim |\mathbf{k}_\parallel|^2$ can function as a "lens," which has a very different mechanism for focusing and imaging. Unlike lenses that are spatially variant, such a "lens" can be spatially homogeneous with no specific geometric center. As long as $u < \tilde{f} - l$ (l: the thickness of the lens), the image of the source will appear on the opposite side of the reciprocal lens and thus will be real. Moreover, the image of an object produced by this kind of lens will be upright as the directions of the rays remain unchanged.

We refer to this class of "lenses" as "reciprocal lenses" for two reasons: First, the distance between the source and the image is a constant, leading to a different lens formula,

$$u + v = \tilde{f}. \tag{5}$$

The form of this lens formula [Eq. (5)] is the reciprocal of the well-known Gaussian lens formula $1/u + 1/v = 1/f$. As such, while reciprocal lenses cannot focus incoming waves from infinitely distant objects, they are well suited for near-field imaging of objects in close proximity to the lens plane. The phase distribution function [Eq. (4)] is also the reciprocal of that of lenses [Eq. (2)]. Note that $\tilde{f}$ in Eq. (5) plays a similar role to the focal length f if we compare the formula with the Gaussian one. Thus, we can define $\tilde{f}$ as the focal length of a reciprocal lens.

Second and most importantly, reciprocal lenses are based on the ray-shifting effect we derived, which is the reciprocal counterpart effect of ray bending. Rather than changing $\theta(x)$, the propagation directions of rays at different positions, reciprocal lenses modulate $x(\theta)$, the positions of rays with different incident angles. The roles of x and θ (or k_x) are exchanged.

Conceptually, slabs supporting negative refraction can be viewed as examples of reciprocal lenses [21–31], as illustrated in Fig. 1 (Veselago-Pendry lenses). An arbitrary ray will be bent twice on passing through the slab, effectively resulting in a shift that corresponds to the z-direction propagation phase gained by the ray. The focal length $\tilde{f}$ of such a slab is $l(1 - n_0/n_1)$, where l is the thickness of the slab, n_0 is the background refractive index, and n_1 is the refractive index of the slab. When a reciprocal lens based on negative refraction is combined with the evanescent-wave-amplification effect, subwavelength imaging can be realized in the near field [23,25,28]. Different materials including indefinite media and hyperbolic metamaterials have been proposed to realize negative refraction lenses [32–37]. However, there are difficulties in realizing a bulky slab with negative refraction [29,30]. For example, achieving 3D all-angle negative refraction typically necessitates the use of intricate structures [38–40]. Moreover, producing reciprocal lenses based on negative refraction still entails bending rays at the interfaces, and the displacement of rays depends on the propagation phase given by a slab that is thick enough so that the bulk dispersion is well defined. As a result, such a lens may occupy a significant amount of space in the optical path, potentially leading to practical limitations.

IV. REALIZATION OF AN ULTRATHIN RECIPROCAL LENS

In this work, we eliminate the bulky structure and realize a reciprocal lens based on the ray-shifting effect only. Instead of leveraging the propagation phase, we apply guided resonances supported by a two-dimensional (2D) photonic crystal (PhC) slab [41–47] to induce the momentum-space phase modulation, which allows the resulting reciprocal lens to be ultrathin. When the incident and outgoing polarization states of the plane waves passing through the PhC slab are the same (copolarization condition), it can be shown that a specific photonic band of guided resonances could give approximately a $|\mathbf{k}_\parallel|^2$-dependent resonant phase modulation to the transmitted waves with $\mathbf{k}_\parallel \approx \mathbf{0}$ [45,47]. The derivations and discussions of the transmissive phase induced by a 2D PhC slab are detailed in Appendix A. If the phase modulation meets the requirements that it is positively quadratic and sufficiently isotropic, the PhC slab will behave like a reciprocal lens. The operation of a 2D PhC slab does not require a precisely defined 3D bulk dispersion, and its functionality is not contingent on effective medium theory. As a result, it offers advantages over negative refraction lenses, which require both (more information can be found in Appendix D). Note that such an ultrathin reciprocal lens cannot recover the evanescent waves carrying subwavelength information; therefore, it cannot perform subdiffraction-limit imaging.

We designed and fabricated a 2D-PhC-slab reciprocal lens operating in the microwave range using printed circuit boards (PCBs). As shown in Fig. 2(a), a one-millimeter-thick PCB (permittivity: 6.15; loss tangent: 0.002) structured with circular holes and printed with hexagonal metallic patches acts as the core 2D-PhC-slab layer. The holes are arranged periodically in a honeycomb array, and the distance between two neighboring holes r_{cell} is 3.648 mm. In each unit cell, there is a patch in the middle of the six holes on each side of the PCB. Such a lattice is C_{6v} symmetric. The structured core layer supports both transverse-electric-like (TE-like) and transverse-magnetic-like (TM-like) guided resonances as a result of the Bragg scattering of the periodic array, which is necessary in our design for momentum-space phase modulation. The core layer is clad by two background layers (thickness: 4.725 mm; permittivity: 2.2; loss tangent: 0.0009), taking the possibility of multilayer stacking into consideration.

In our experiments, the input and output waves are chosen to both be left-handed (or right-handed) circularly polarized. Combining the circular symmetry of the polarization states and the C_{6v} symmetry of the structure, the system is C_6 symmetric, which guarantees good isotropic phase modulation provided by the reciprocal lens in the momentum space. It can be seen from the measured angle-resolved phase spectra [right panel of Fig. 2(b)] that the momentum-space phase modulation of the reciprocal lens is nearly the same for the two different high-symmetry directions Γ-K and Γ-M near $\mathbf{k}_\parallel = \mathbf{0}$. Note that the momentum-space-variant transmittance at the working frequency also affects the quality of focusing and imaging. In order for the transmittance to approach unity and to have a large enough phase span, we tune the radii of the holes

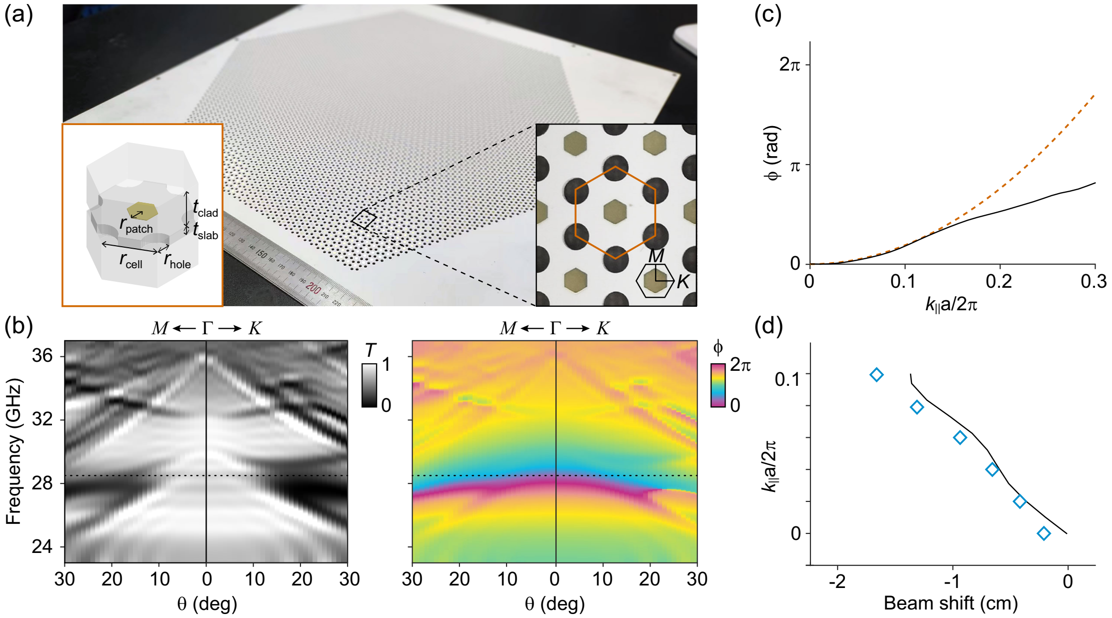

FIG. 2. Characteristics of the designed ultrathin reciprocal lens. (a) Photo of the core layer of the designed reciprocal lens comprising a honeycomb array of circular holes etched on a PCB, whose permittivity is 6.15 and loss tangent is 0.002 (Arlon TC600). A hexagonal metallic patch is printed at the center of each honeycomb unit cell. The structured PCB acts as a photonic crystal slab and is clad by two background layers (Arlon DiClad 880, permittivity: 2.2; loss tangent: 0.0009). Left inset: schematics of the unit cell. Right inset: zoomed-in photo of the structure. (b) Angle-resolved transmittance and transmissive phase-change spectra of the structure (with circularly copolarized input and output). (c) Phase-change curve along the Γ-K direction at a working frequency of 28.5 GHz. In a specific wave-vector (angle) range, the phase induced by the reciprocal lens (solid curve) follows the quadratic rule we desired, of which the fitted quadratic dependence is plotted as the dashed curve. (d) Beam shifts for different incident angles corresponding to the momentum-space phase gradient. The shifts of the beam centroids for different incident angles (blue diamonds) follow the displacements calculated from the momentum-space phase gradients (black curve). It can be seen that the beam shift has the expected linear dependence on the in-plane wave vector.

(r_{hole}: 1.113 mm) and the patches (r_{patch}: 1.094 mm), respectively. Consequently, one pair of TE-like degenerate resonances overlap with another pair of TM-like resonances in the spectrum, leading to a high copolarized transmittance [48–50]. Detailed discussions about enhancing the transmittance by overlapping degenerate resonances can be found in Appendixes B and C. As shown in the left panel of Fig. 2(b), the measured transmittance is high near $\mathbf{k}_{\|} = \mathbf{0}$ (in about the 10 degrees range) over a moderate spectral range.

We choose a working frequency of 28.5 GHz [marked by a dashed line in Fig. 2(b)], where the momentum-space phase distribution best fits the positive quadratic dependence and gives the greatest focal length. The $\mathbf{k}_{\|}$ phase modulation function along the Γ-K direction at the working frequency is measured and plotted in Fig. 2(c). As mentioned, the phase induced by the structure follows the quadratic rule over a specific range of $\mathbf{k}_{\|}$. By curve fitting, we find that the focal length $\tilde{f}$ at 28.5 GHz is about 7–8 cm, which is nearly 7 times the wavelength. In addition, we measure the shift of a Gaussian beam (waist radius of about 4.57 cm) with different central wave vectors in the sample plane, which is plotted in Fig. 2(d). The incident in-plane wave vectors are chosen to be in the Γ-K direction. The beam shifts confirm that the momentum-space phase modulations induced by the designed structure can shift rays in the expected way as illustrated in Fig. 1 and described by Eq. (4); i.e., it can work as a reciprocal lens. Constrained by the high-transmittance region in momentum space, we estimate the resolution of our reciprocal lens to be about 3.2 cm in the focal plane.

As shown in Fig. 3, we demonstrate the imaging effect of the designed ultrathin reciprocal lens by measuring the transmitted field pattern directly. We use a metallic plate with an “F”-shaped slot cut in it as the imaging object, which is shown in Fig. 3(a). The object is set at a position marked as $z = 0$, and the slot is illuminated uniformly by a horn antenna. First, one layer of the designed reciprocal lens is placed at $z = 3$ cm. Consequently, we observe a clear, upright, real image of the object “F” slot at $z = 7.5$ cm with sharp boundary profiles [Fig. 3(c)]. The image is the same size as the object. For comparison, a diffracted pattern of the object is seen if the reciprocal lens is removed.

In addition, reciprocal lenses can be stacked to increase the focal length. By stacking multiple identical reciprocal lenses, the momentum-space phase modulation may be enlarged additively, giving a focal length several times the

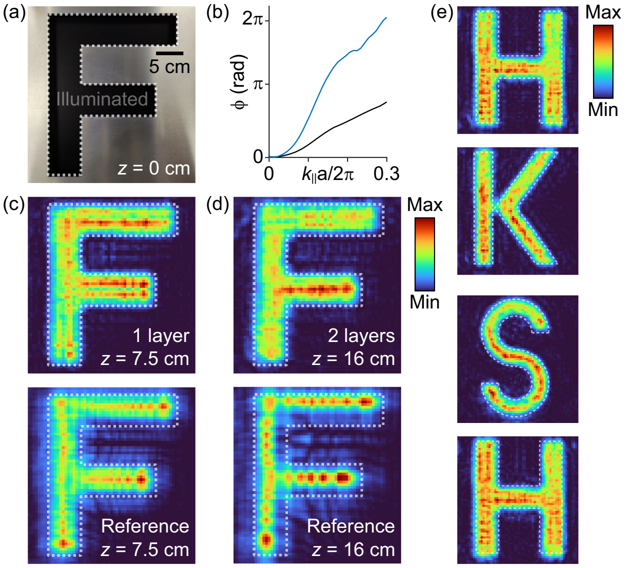

FIG. 3. Imaging by reciprocal lens. (a) The “$z = 0$ cm” photo showing the object, which is a metallic plate with an “F”-shaped slot cut into it. A horn antenna is used to illuminate the slot. (b) Measured transmissive phase distributions for the one-layered (black curve) and two-layered (blue curve) reciprocal lenses. (c) One layer of our designed reciprocal lens applied at $z = 3$ cm, where an upright real image of the “F”-slot can be seen clearly at $z = 7.5$ cm. In comparison, only a diffracted pattern can be seen without the reciprocal lens. (d) Two layers of the designed reciprocal lens cascaded to increase the focal length to about 15–16 cm. (e) Several different shapes of objects used to demonstrate the imaging effect.

original one. To demonstrate this fact, we apply two layers of the designed reciprocal lens placed at $z = 8$ cm, stacked immediately on top of each other. We note that the thickness of the cladding layers has been chosen to reduce the interaction between the photonic crystal slabs in the stacked reciprocal lens. If we simply stack the photonic crystal slabs on top of each other without the spacers, the interaction between the resonances of adjacent photonic crystal slabs may affect the total transmittance and transmissive phase so that the focal length will not be additive and may degrade the performance of the stacked reciprocal lens. From the measured momentum-space phase distribution [Fig. 3(b)], we find that the phase modulation is nearly doubled, leading to a focal length of about 15–16 cm. We confirm the increased focal length by measuring the field profile as well. The image produced at $z = 16$ cm is of good quality, while the field without the stacked reciprocal lens at $z = 16$ cm is more strongly diffracted [Fig. 3(d)]. We also used several different shapes of objects, such as “H,” “K,” and “S,” to further test the imaging effect of the one-layer reciprocal lens. All the shapes are well imaged, as shown in Fig. 3(e). The acute angles of “K” and curved edges of “S” are well reproduced in the images, indicating that there is no constraint on the shape of objects. The two images of the “H”-shaped slot, which are obtained from separate imaging tests, appear to be almost identical, proving the imaging repeatability. The detailed experimental setups can be found in Appendix E.

V. CONCLUSIONS

In summary, we have introduced and experimentally demonstrated the concept of the PhC-slab-based “reciprocal lens,” a novel imaging component that produces upright but real images without bending rays. Unlike conventional lenses and metalenses, our reciprocal lens has no geometric center and the object-image distance is a constant. Composed of an ultrathin periodic structure, our reciprocal lens is not only simple to fabricate but also easy to integrate, and it can image multiple objects simultaneously due to its nonlocality. The reciprocal lens based on a PhC slab presents a novel paradigm, which adds to the array of optical elements available for imaging and wavefront reshaping. These lenses have potential applications in niche areas, such as volume-to-volume imaging and optical image stabilization. These applications can be realized by reducing the cost of reciprocal lenses with an optical building block technique, enhancing their performance with optimization algorithms, and refining optical range fabrication methods. Looking forward, by incorporating additional forms of momentum-space modulation, such as those used for phase contrast [51–54] or edge visualization imaging [55–57], it may be possible to integrate multiple functionalities into a single photonic crystal reciprocal lens design. Furthermore, this breakthrough can serve as inspiration for other types of ray-shifting-based optical devices, such as spectrometers.

ACKNOWLEDGMENTS

This work is supported by the Research Grants Council of Hong Kong through Grant No. AoE/P-502/20, the Croucher Foundation (CAS20SC01), National Natural Science Foundation of China (No. 12234007 and No. 12221004), National Key Research and Development Program of China (2021YFA1400603, 2022YFA1404800), and Major Program of National Natural Science Foundation of China (91963212). L. S. is further supported by Science and Technology Commission of Shanghai Municipality (22142200400, 21DZ1101500 and 2019SHZDZX01).

W. L., J. C., and T. L. contributed equally to this work.

APPENDIX A: MOMENTUM-SPACE PHASE MODULATION INDUCED BY A PHOTONIC BAND OF GUIDED RESONANCES

First, let us consider a single-resonance temporal coupled mode theory (TCMT) [58] of a periodic structure with in-plane wave vector $\mathbf{k}_{\parallel}$. The system is considered to have σ_z about the x-y plane and C_{2v} symmetry about the z axis. No diffractive radiation is involved, and since the system has a C_2 symmetry, it is not necessary for us to take the $-\mathbf{k}_{\parallel}$ resonance into consideration. As a result, there will be four channels to consider ($\pm\mathbf{k_z}$ and two orthogonal polarization states). Thus, we can write the TCMT equations:

$$\begin{aligned}\frac{d}{dt}|A\rangle &= (-i\mathbf{\Omega_0}-\mathbf{\Gamma_0})|A\rangle+\mathbf{K}^{\mathrm{T}}|\mathrm{in}\rangle,\\ |\mathrm{out}\rangle &= \mathbf{S}|\mathrm{in}\rangle=\mathbf{C}|\mathrm{in}\rangle+\mathbf{D}|A\rangle.\end{aligned}\tag{A1}$$

In the first equation, $|A\rangle = A$ is the resonance amplitude, $\mathbf{\Omega_0}=\omega_0$ is the resonant frequency of the resonance, and $\mathbf{\Gamma_0}=\gamma_0$ is the decay rate. Since the system works in the microwave range, the metallic parts of the structure can be considered lossless. Therefore, γ_0 corresponds to the radiation loss. The vector $\mathbf{K}=(k_a^u,k_a^d,k_b^u,k_b^d)^{\mathrm{T}}=(k_a,\alpha_z k_a,k_b,\alpha_z k_b)^{\mathrm{T}}$ is the coupling coefficient between the resonance and the ingoing plane waves on an arbitrary orthogonal polarization basis (a,b), where $\alpha_z=\pm1$ is a parity number linking the upside radiation and the downside radiation because of the sample-plane mirror symmetry. We will explain $|\mathrm{in}\rangle$ below.

In the second equation, $|\mathrm{in}\rangle$ and $|\mathrm{out}\rangle$ are the input and output amplitude vectors, $\mathbf{C}$ is the direct amplitude scattering matrix without the influence of the resonance, $\mathbf{S}$ is the resonance-involved amplitude scattering matrix of the structure, and $\mathbf{D}$ is the coupling coefficient between the resonance and the outgoing plane waves. The detailed forms of the vectors and matrices are

$$|\mathrm{in}\rangle=\begin{pmatrix}\mathrm{in}_a^u\\ \mathrm{in}_a^d\\ \mathrm{in}_b^u\\ \mathrm{in}_b^d\end{pmatrix},\quad |\mathrm{out}\rangle=\begin{pmatrix}\mathrm{out}_a^u\\ \mathrm{out}_a^d\\ \mathrm{out}_b^u\\ \mathrm{out}_b^d\end{pmatrix},$$

$$\mathbf{C}=\begin{pmatrix}r_{aa}&t_{aa}&r_{ab}&t_{ab}\\ t_{aa}&r_{aa}&t_{ab}&r_{ab}\\ r_{ba}&t_{ba}&r_{bb}&t_{bb}\\ t_{ba}&r_{ba}&t_{bb}&r_{bb}\end{pmatrix},\quad \mathbf{S}=\begin{pmatrix}\tilde{r}_{aa}&\tilde{t}_{aa}&\tilde{r}_{ab}&\tilde{t}_{ab}\\ \tilde{t}_{aa}&\tilde{r}_{aa}&\tilde{t}_{ab}&\tilde{r}_{ab}\\ \tilde{r}_{ba}&\tilde{t}_{ba}&\tilde{r}_{bb}&\tilde{t}_{bb}\\ \tilde{t}_{ba}&\tilde{r}_{ba}&\tilde{t}_{bb}&\tilde{r}_{bb}\end{pmatrix},$$

$$\mathbf{D}=\begin{pmatrix}d_a\\ \alpha_z d_a\\ d_b\\ \alpha_z d_b\end{pmatrix}.\tag{A2}$$

Note that we have a specific natural polarization basis (p,s) under which $t_{ps}(r_{ps})$ and $t_{sp}(r_{sp})$ vanish, considering the physics of the direct scattering process. Furthermore, the difference between $t_{pp}(r_{pp})$ and $t_{ss}(r_{ss})$ can be approximately neglected if the incident angle is small.

The system is energy conserved and has a time-reversal symmetry. Consequently, we have several equations:

$$\mathbf{D}^{\dagger}\mathbf{D}=2\gamma_0,\qquad \mathbf{C}\mathbf{D}^{*}=-\mathbf{D},\qquad \mathbf{K}=\mathbf{D}.\tag{A3}$$

The first equation gives us

$$|d_a|^2+|d_b|^2=\gamma_0.\tag{A4}$$

On the (p,s) basis, the second equation gives some extra insights:

$$\begin{aligned}&\frac{d_s}{d_s^*}=-(r_{ss}+\alpha_z t_{ss}),\qquad \frac{d_p}{d_p^*}=-(r_{pp}+\alpha_z t_{pp}),\\ &|r_{pp,ss}+\alpha_z t_{pp,ss}|=1,\\ &t_{pp,ss}r_{pp,ss}^*\in\mathbb{I},\qquad t_{pp,ss}/r_{pp,ss}\in\mathbb{I}.\end{aligned}\tag{A5}$$

In the vicinity of the Γ point (normal incident inputs and outputs), $r_s+\alpha_z t_s\approx r_p+\alpha_z t_p$. Therefore, the phase difference between d_s and d_p is close to zero in this case. In other words, the polarization eigenstate of radiation of the resonance shall be almost linear.

Given a real frequency ω, we can solve Eq. (A1) for the scattering matrix,

$$\mathbf{S}=\mathbf{C}+\frac{\mathbf{D}\mathbf{K}^{\mathrm{T}}}{i(\omega_0-\omega)+\gamma_0}.\tag{A6}$$

We can straightforwardly write down the copolarized transmission coefficient:

$$\begin{aligned}\tilde{t}_{ii}&=t_{ii}+\frac{\alpha_z d_i^2}{i(\omega_0-\omega)+\gamma_0}=t_{ii}\frac{i(\omega_0-\omega)+\gamma_0+\frac{\alpha_z d_i^2}{t_{ii}}}{i(\omega_0-\omega)+\gamma_0}\\ &=t_{ii}\frac{i(\omega_0-\omega)+\gamma_0-[(\alpha_z\frac{r_{ii}}{t_{ii}}+1)|d_i|^2+(\alpha_z\frac{r_{ij}}{t_{ii}}+\frac{t_{ij}}{t_{ii}})d_i d_j^*]}{i(\omega_0-\omega)+\gamma_0}.\end{aligned}\tag{A7}$$

As mentioned, we assume near normal incidence. In such a case, we neglect the difference between $t_{pp}(r_{pp})$ and $t_{ss}(r_{ss})$, and assume $t_{pp}=t_{ss}=t, r_{pp}=r_{ss}=r$. Then, the cross-polarized transmission coefficients in any basis will be zero, while $t_{ii}=t_{jj}=t, r_{ii}=r_{jj}=r$. As a result, Eq. (A7) can be simplified to

$$\tilde{t}_{ii}\approx t\frac{i(\omega_0-\omega)+\gamma_0-(\alpha_z r/t+1)|d_i|^2}{i(\omega_0-\omega)+\gamma_0}.\tag{A8}$$

For convenience, we define two real numbers to simplify the equation, $p=|d_i|^2/\gamma_0^2\in[0,1]$ and $q=-ir/t\in[-\infty,+\infty]$. Subsequently, Eq. (A8) can be rewritten as

$$\begin{aligned}\tilde{t}_{ii} &\approx t\frac{i(\omega_0-\omega)+\gamma_0-(i\alpha_z q+1)p\gamma_0}{i(\omega_0-\omega)+\gamma_0}\\ &= t\frac{i(\frac{\omega_0-\omega}{\gamma_0}-\alpha_z pq)+(1-p)}{i\frac{\omega_0-\omega}{\gamma_0}+1}.\end{aligned} \tag{A9}$$

Thus, the copolarized transmissive phase is composed of three parts, ϕ_1, ϕ_2, and ϕ_3:

$$\begin{aligned}\phi &= \arg(\tilde{t}_{ii}) = \phi_1+\phi_2+\phi_3\\ &= \arg(t)+\arg\left[(1-p)+i\left(\frac{\omega_0-\omega}{\gamma_0}-\alpha_z pq\right)\right]\\ &\quad -\arg\left(1+i\frac{\omega_0-\omega}{\gamma_0}\right).\end{aligned} \tag{A10}$$

The first part of Eq. (A10) corresponds to the direct transmission. This part is obviously an even function of the in-plane wave vector $\mathbf{k}_\parallel$ and varies slowly. We can assume it to be

$$\phi_1(\omega, k_\parallel) \approx c_1 k_\parallel^2 + c_0, \tag{A11}$$

where c_1 is a small, positive, real constant. For the second and third parts, there are ω_0-related terms bringing in momentum-space dispersions. It is known that photonic bands formed by guided resonances generally have quadratic dispersions along different azimuthal directions near high-symmetry points like the Γ point, i.e.,

$$\omega_0(k_\parallel) \approx \omega_e + c_2 k_\parallel^2 \ (k_\parallel \approx 0). \tag{A12}$$

Here, $\omega_e = \omega_0(0)$. By a Taylor series expansion with the assumption $p \neq 1$, we obtain

$$\begin{aligned}\phi_2(\omega, k_\parallel) &\approx \arg\left[(1-p)+i\left(\frac{\omega_e-\omega}{\gamma_0}-\alpha_z pq\right)\right]\\ &\quad + \frac{\gamma_0(1-p)c_2 k_\parallel^2}{\gamma_0^2(1-p)^2+(\omega_e-\omega-\alpha_z pq\gamma_0)^2},\\ \phi_3(\omega, k_\parallel) &\approx -\arg\left[1+i\left(\frac{\omega_e-\omega}{\gamma_0}\right)\right]-\frac{\gamma_0 c_2 k_\parallel^2}{\gamma_0^2+(\omega_e-\omega)^2}.\end{aligned} \tag{A13}$$

Hence, we substitute Eqs. (A11) and (A13) into Eq. (A10) to obtain

$$\begin{aligned}\phi(\omega,k_\parallel) \approx \phi(\omega,0) + \Bigg[c_1 &+ \frac{\gamma_0(1-p)c_2}{\gamma_0^2(1-p)^2+(\omega_e-\omega-\alpha_z pq\gamma_0)^2}\\ &- \frac{\gamma_0 c_2}{\gamma_0^2+(\omega_e-\omega)^2}\Bigg]k_\parallel^2.\end{aligned} \tag{A14}$$

As long as $p \neq 0$ (in other words, the input polarization state is not perpendicular to the polarization eigenstate of the resonance and hence does not excite the resonance), the resonant phase terms will not cancel each other.

If the photonic band considered does not have bound states in the continuum (BICs) near (or at) the Γ point, γ_0 should vary slowly with $k_\parallel$. Here, p corresponds to how strongly the resonance is excited by the incidence, and it will not be strongly dependent on $k_\parallel$ when the azimuthal angle of $\mathbf{k}_\parallel$ is fixed. Note that q is stable in a moderate range of ω and $k_\parallel$, and c_1, c_2 are constants along a specific azimuthal direction of $\mathbf{k}_\parallel$. On the other hand, ω, ω_e, and α_z are all constants. As such, the quadratic coefficient can be viewed as a constant. Now, we can conclude that a photonic band of guided resonances can give a momentum-space phase modulation with a quadratic dependence in a specific azimuthal direction of $\mathbf{k}_\parallel$. Usually, c_1 in an ultrathin dielectric structure is small, and the resonance-induced quadratic phase modulation dominates. A negative c_2 should give a positive quadratic phase modulation, which is necessary for a reciprocal lens.

APPENDIX B: ENHANCING TRANSMITTANCE BY OVERLAPPING TWO PAIRS OF DEGENERATE STATES

We mention that if only one photonic band of guided resonances is applied, the efficiency of the copolarized transmission will be pretty low when ω is close to $\omega_0(k_\parallel)$. For example, if $p = 1$ (the input polarization state is parallel to the polarization eigenstate of the resonance) and $\omega = \omega_0 - \alpha_z q\gamma_0$ in Eq. (A8), the copolarized transmission coefficient will become 0. Moreover, we know that polarization eigenstates of guided resonances supported by a photonic crystal slab are almost linear in the vicinity of the Γ point when the system has a C_2 symmetry. Without an at-Γ BIC, the momentum-space distribution of polarization eigenstates on a single photonic band in such a case can only have a C_{2v} symmetry at most [59,60]. As a result, the order of rotational symmetry of a phase modulation given by a single photonic band cannot exceed 2. In other words, the phase modulation will be anisotropic, in general. These are not ideal for the realization of a reciprocal lens.

There are two key points to overcome these disadvantages. First, we need to remove the low-efficiency regions. In order to accomplish that, we can apply multiple resonances overlapping in the spectral range (degeneracies). The form of the transmission coefficient would be different. Second, we expect the system to have higher-order symmetries. With degeneracies, the polarization eigenstate distribution on a photonic band can have sixfold rotational symmetry at the maximum without involving a BIC [59,60]. We can further apply input and output polarization states, which have higher-order rotational symmetries, as well to match with the rotational symmetry of the polarization eigenstates. As such, the system can have higher-order symmetries. The best choice of the input (output) beam's polarization is the circular polarization if we do not take vector beams into account.

Here, let us construct the multiresonance TCMT on the circular polarization basis. We start from a two-resonance configuration with a Γ-point radiative degeneracy that is protected by a C_{6v} symmetry. Now, $|A\rangle$ is a 2×1 column vector $(A_{\mathrm{I}}, A_{\mathrm{II}})^{\mathrm{T}}$. Correspondingly, $\mathbf{D}$ and $\mathbf{K}$ are 4×2 matrices:

$$\mathbf{D} = \mathbf{K} = \begin{pmatrix} d_r^{\mathrm{I}} & d_r^{\mathrm{II}} \\ \alpha_z d_r^{\mathrm{I}} & \alpha_z d_r^{\mathrm{II}} \\ d_l^{\mathrm{I}} & d_l^{\mathrm{II}} \\ \alpha_z d_l^{\mathrm{I}} & \alpha_z d_l^{\mathrm{II}} \end{pmatrix}. \tag{B1}$$

Meanwhile, we suppose that the eigenfrequency matrix $\mathbf{\Omega_0}$ and the decay ratio matrix $\mathbf{\Gamma_0}$ are 2×2 diagonal matrices on an orthogonal basis:

$$\mathbf{\Omega_0} = \begin{pmatrix} \omega_0^{\mathrm{I}} & 0 \\ 0 & \omega_0^{\mathrm{II}} \end{pmatrix}, \qquad \mathbf{\Gamma_0} = \begin{pmatrix} \gamma_0^{\mathrm{I}} & 0 \\ 0 & \gamma_0^{\mathrm{II}} \end{pmatrix}. \tag{B2}$$

Note that the above assumption implies $d_r^i d_r^{j*} + d_l^i d_l^{j*} = 0$; i.e., the polarization eigenstates of the two resonances are orthogonal to each other. This is true for resonances in the vicinity of the degeneracy in momentum space.

Still assuming $t_{pp} = t_{ss} = t, r_{pp} = r_{ss} = r$, we can write down the new form of the copolarized transmission coefficient:

$$\tilde{t}_{ii} \approx t - \frac{(\alpha_z r + t)|d_i^{\mathrm{I}}|^2}{i(\omega_0^{\mathrm{I}} - \omega) + \gamma_0^{\mathrm{I}}} - \frac{(\alpha_z r + t)|d_i^{\mathrm{II}}|^2}{i(\omega_0^{\mathrm{II}} - \omega) + \gamma_0^{\mathrm{II}}} \quad (i = l, r). \tag{B3}$$

Note that we here have a Γ-point degeneracy. Therefore, the two bands have the same ω_0 and γ_0 at the Γ point. Their approximate expressions will be

$$\begin{aligned} &\omega_0^{\mathrm{I}}(k_\parallel) \approx \omega_e + c_2^{\mathrm{I}} k_\parallel^2, \qquad \omega_0^{\mathrm{II}}(k_\parallel) \approx \omega_e + c_2^{\mathrm{II}} k_\parallel^2, \\ &\gamma_0^{\mathrm{I}}(k_\parallel) \approx \gamma_0^{\mathrm{II}}(k_\parallel) \approx \gamma_0(k_\parallel \approx 0). \end{aligned} \tag{B4}$$

Note that the polarization eigenstates of the resonances are almost linear. On the circular polarization basis, this means that

$$p_i^{\mathrm{I}} = |d_i^{\mathrm{I}}|^2/\gamma_0 \approx 1/2, \qquad p_i^{\mathrm{II}} = |d_i^{\mathrm{II}}|^2/\gamma_0 \approx 1/2. \tag{B5}$$

We have

$$\tilde{t}_{ii} \approx t \frac{-2c_2^{\mathrm{I}} c_2^{\mathrm{II}} k_\parallel^4 + i(c_2^{\mathrm{I}} + c_2^{\mathrm{II}})[\gamma_0 - iq\alpha_z\gamma_0 - 2i(\omega - \omega_e)]k_\parallel^2 - 2i[q\alpha_z\gamma_0 + (\omega - \omega_e)][\gamma_0 - i(\omega - \omega_e)]}{2[\gamma_0 - i(\omega - \omega_e - c_2^{\mathrm{I}} k_\parallel^2)][\gamma_0 - i(\omega - \omega_e - c_2^{\mathrm{II}} k_\parallel^2)]}. \tag{B6}$$

We find that when $k_\parallel = 0$, $\tilde{t}_{ii}$ will be

$$\tilde{t}_{ii}(0) = -t \frac{iq\alpha_z\gamma_0 + i(\omega - \omega_e)}{\gamma_0 - i(\omega - \omega_e)}, \tag{B7}$$

which is a typical Fano line-shape function with an inevitable zero point. This is not the result we want. However, we have removed the terms containing p that may induce strong anisotropy to the momentum-space phase modulation given by the PhC slab.

The transmissive phase can be divided into four parts:

$$\begin{aligned} \phi_1(\omega, k_\parallel) &= \arg(t) \approx c_1 k_\parallel^2 + c_0, \\ \phi_2(\omega, k_\parallel) &\approx \arg\left[1 + i\left(\frac{\omega_e - \omega}{\gamma_0}\right)\right] + \frac{1}{2}\frac{(c_2^{\mathrm{I}} + c_2^{\mathrm{II}})\gamma_0 k_\parallel^2}{\gamma_0^2 + (\omega - \omega_e)^2} - \frac{\pi}{2}\mathrm{sgn}\left[q\alpha_z\gamma_0 - \frac{2(\omega_e + c_2^{\mathrm{I}} k_\parallel^2 - \omega)(\omega_e + c_2^{\mathrm{II}} k_\parallel^2 - \omega)}{2\omega_e + c_2^{\mathrm{I}} k_\parallel^2 + c_2^{\mathrm{II}} k_\parallel^2 - 2\omega}\right], \\ \phi_3(\omega, k_\parallel) &\approx -\arg\left[1 + i\left(\frac{\omega_e - \omega}{\gamma_0}\right)\right] - \frac{c_2^{\mathrm{I}}\gamma_0 k_\parallel^2}{\gamma_0^2 + (\omega - \omega_e)^2}, \\ \phi_4(\omega, k_\parallel) &\approx -\arg\left[1 + i\left(\frac{\omega_e - \omega}{\gamma_0}\right)\right] - \frac{c_2^{\mathrm{II}}\gamma_0 k_\parallel^2}{\gamma_0^2 + (\omega - \omega_e)^2}. \end{aligned} \tag{B8}$$

Thus, the total transmissive phase is

$$
\begin{aligned}
\phi(\omega, k_{\|}) \approx c_0 - \arg\left[1 + i\left(\frac{\omega_e - \omega}{\gamma_0}\right)\right] - \frac{\pi}{2}\operatorname{sgn}\left[q\alpha_z\gamma_0 - \frac{2(\omega_e + c_2^{\mathrm{I}}k_{\|}^2 - \omega)(\omega_e + c_2^{\mathrm{II}}k_{\|}^2 - \omega)}{2\omega_e + c_2^{\mathrm{I}}k_{\|}^2 + c_2^{\mathrm{II}}k_{\|}^2 - 2\omega}\right] \\
+ \left[c_1 - \frac{1}{2}\frac{(c_2^{\mathrm{I}} + c_2^{\mathrm{II}})\gamma_0}{\gamma_0^2 + (\omega - \omega_e)^2}\right]k_{\|}^2. \qquad \text{(B9)}
\end{aligned}
$$

Note that the quadratic dependence is still present.

In the next step, we apply more resonances to remove the zero point. We add two other resonances with a Γ-point degeneracy, whose *x*-*y*-plane mirror parity is different from the ones discussed. For simplicity, we assume that this pair of resonances has the same dispersion as the aforementioned pair. The matrices would be

$$
\mathbf{D} = \mathbf{K} = \begin{pmatrix} d_r^{\mathrm{I}} & d_r^{\mathrm{II}} & d_r^{\mathrm{I}} & d_r^{\mathrm{II}} \\ d_r^{\mathrm{I}} & d_r^{\mathrm{II}} & -d_r^{\mathrm{I}} & -d_r^{\mathrm{II}} \\ d_l^{\mathrm{I}} & d_l^{\mathrm{II}} & d_l^{\mathrm{I}} & d_l^{\mathrm{II}} \\ d_l^{\mathrm{I}} & d_l^{\mathrm{II}} & -d_l^{\mathrm{I}} & -d_l^{\mathrm{II}} \end{pmatrix},
$$

$$
\mathbf{\Omega_0} = \begin{pmatrix} \omega_0^{\mathrm{I}} & 0 & 0 & 0 \\ 0 & \omega_0^{\mathrm{II}} & 0 & 0 \\ 0 & 0 & \omega_0^{\mathrm{I}} & 0 \\ 0 & 0 & 0 & \omega_0^{\mathrm{II}} \end{pmatrix},
$$

$$
\mathbf{\Gamma_0} = \begin{pmatrix} \gamma_0 & 0 & 0 & 0 \\ 0 & \gamma_0 & 0 & 0 \\ 0 & 0 & \gamma_0 & 0 \\ 0 & 0 & 0 & \gamma_0 \end{pmatrix}. \qquad \text{(B10)}
$$

We obtain the expression of the copolarized transmission coefficient:

$$
\begin{aligned}
t_{ii} &\approx t\left[1 - \frac{\gamma_0}{\gamma_0 - i(\omega - \omega_e - c_2^{\mathrm{I}}k_{\|}^2)} - \frac{\gamma_0}{\gamma_0 - i(\omega - \omega_e - c_2^{\mathrm{II}}k_{\|}^2)}\right] \\
&= t\frac{-c_2^{\mathrm{I}}c_2^{\mathrm{II}}k_{\|}^4 + (c_2^{\mathrm{I}} + c_2^{\mathrm{II}})(\omega - \omega_e)k_{\|}^2 - (\omega - \omega_e)^2 - \gamma_0^2}{[\gamma_0 - i(\omega - \omega_e - c_2^{\mathrm{I}}k_{\|}^2)][\gamma_0 - i(\omega - \omega_e - c_2^{\mathrm{II}}k_{\|}^2)]}. \qquad \text{(B11)}
\end{aligned}
$$

The direct reflection coefficient *r* disappears from the expression when we overlap the two pairs of resonances. The squared modulus of t_{ii} would be

$$
\begin{aligned}
&|t_{ii}(\omega, k_{\|})|^2 \\
&\quad = |t|^2\frac{[\gamma_0^2 + (\omega_e + c_2^{\mathrm{I}}k_{\|}^2 - \omega)(\omega_e + c_2^{\mathrm{I}}k_{\|}^2 - \omega)]^2}{[\gamma_0^2 + (\omega_e + c_2^{\mathrm{I}}k_{\|}^2 - \omega)^2][\gamma_0^2 + (\omega_e + c_2^{\mathrm{I}}k_{\|}^2 - \omega)^2]}. \qquad \text{(B12)}
\end{aligned}
$$

Clearly, Eq. (B11) is no longer a Fano line-shape function. The fraction on the right side of Eq. (B12) is close to unity when $k_{\|}$ is small and will reach 1 with $k_{\|} = 0$. Meanwhile, if the structure is mainly composed of dielectric material, $|t|$ can easily be tuned to approach 1 as well. The numerator can still give zero-amplitude points but only when

$$
\begin{aligned}
&|k_{\|}|^2 > \frac{2\gamma_0}{|c_2^{\mathrm{I}} - c_2^{\mathrm{II}}|} \\
&\qquad \text{and} \\
&\omega = \omega_e + \frac{1}{2}(c_2^{\mathrm{I}} + c_2^{\mathrm{II}})k_{\|}^2 \pm \frac{1}{2}\sqrt{(c_2^{\mathrm{I}} - c_2^{\mathrm{II}})^2k_{\|}^4 - 4\gamma_0^2}. \qquad \text{(B13)}
\end{aligned}
$$

As long as the difference between c_2^{I} and c_2^{II} is small, the zero points will be far away from $k_{\|} = 0$. We have now successfully removed the zero point in the vicinity of $k_{\|} = 0$, achieving a very high efficiency.

We can further look into the phase of Eq. (B11). The numerator gives abrupt $\pm\pi$ phase changes only when Eq. (B13) is satisfied. The main parts contributing to the transmissive phase in this case are *t* and the denominator of the fraction, which will be

$$
\begin{aligned}
&\phi_1(\omega, k_{\|}) = \arg(t) \approx c_1k_{\|}^2 + c_0, \\
&\phi_2(\omega, k_{\|}) \approx -\arg\left[1 + i\left(\frac{\omega_e - \omega}{\gamma_0}\right)\right] - \frac{c_2^{\mathrm{I}}\gamma_0k_{\|}^2}{\gamma_0^2 + (\omega - \omega_e)^2}, \\
&\phi_3(\omega, k_{\|}) \approx -\arg\left[1 + i\left(\frac{\omega_e - \omega}{\gamma_0}\right)\right] - \frac{c_2^{\mathrm{II}}\gamma_0k_{\|}^2}{\gamma_0^2 + (\omega - \omega_e)^2}, \qquad \text{(B14)}
\end{aligned}
$$

and the total phase will be

$$
\begin{aligned}
\phi(\omega, k_{\|}) &\approx c_0 + \pi - 2\arg\left[1 + i\left(\frac{\omega_e - \omega}{\gamma_0}\right)\right] \\
&\quad + \left[c_1 - \frac{(c_2^{\mathrm{I}} + c_2^{\mathrm{II}})\gamma_0}{\gamma_0^2 + (\omega - \omega_e)^2}\right]k_{\|}^2. \qquad \text{(B15)}
\end{aligned}
$$

Compared to Eq. (B9), the quadratic factor of phase modulation given by the resonances is doubled. This is favorable for our realization of a well-performing reciprocal lens.

In conclusion, the above discussions show that we can apply two pairs of resonances (symmetry-protected degeneracies) that have opposite x-y-plane mirror parities (one transverse-electric-like degeneracy and one transverse-magnetic-like degeneracy) but the same ω-$\mathbf{k}_\parallel$ dispersions to enhance the transmission efficiency. In practice, the ω-$\mathbf{k}_\parallel$ dispersions of the two pairs of resonances cannot be identical. However, they can overlap to a certain extent by parameter tuning so that the above discussions are approximately applicable. Furthermore, the existence of degeneracies, along with the choice of circularly polarized input/output polarization states, allows us to design a system with a higher-order rotational symmetry. Making the structure C_{6v} symmetric, the momentum-space phase modulation has a C_6 symmetry, and the quadratic factors c_2^{I} and c_2^{II} of the phase modulation would be nearly isotropic along different azimuthal directions in momentum space. As long as $c_2^{\mathrm{I}} + c_2^{\mathrm{II}}$ is negative, the phase modulation dominated by the resonant phase can be positive quadratic. We can design a PhC-slab-based reciprocal lens with a good performance based on the principles discussed.

APPENDIX C: SIMULATED BAND STRUCTURES OF THE DESIGNED STRUCTURE AND THE CORRESPONDING TRANSMISSION SPECTRA

We designed our reciprocal lens based on the designing principle we discussed in the previous section; the experimental results are shown in the main text. The simulation results are supplemented here in Fig. 4. We modify the radii of the patches (1.058 mm) and holes (1.076 mm) to better match our experimental results. Note that the difference in resonant frequencies may result from the difference between the modeled materials and the practical ones. One can see that the two degeneracies almost overlap in the spectra as we proposed, leading to a high transmittance.

APPENDIX D: DIFFERENCE BETWEEN RESONANCE-BASED RECIPROCAL LENSES AND THE NEGATIVE REFRACTION LENSES

Negative refraction lenses can be viewed as examples of reciprocal lenses. However, our realization of the ultrathin reciprocal lens is different from negative refraction lenses. The difference can be seen in Fig. 5.

As shown in Fig. 5, most realizations of negative-refraction lenses, including slabs made of hyperbolic or indefinite metamaterial, are based on dispersion modification. To be more specific, the metamaterial applied for a negative-refraction lens producing 2D images is designed to have a particular dispersion in 3D momentum space. At a specific frequency, the dispersion appears as a 3D isofrequency surface (k-surface), and such a surface negatively refracts the incident plane waves (rays) at the interface. The refraction angle varies with the incident angle. As a result, negative refraction occurs at the incident interface of the slab and again at the other interface after the propagation of rays inside the slab, effectively leading to different ray displacements. In other words, effective medium theory is used to describe these structures. The modes inside the medium have well-defined plane-wave-like propagations, and it is the optical path length inside the media that causes the ray shifts. As such, to achieve high transmittance and optimal performance, it is necessary that the media have a sufficient thickness.

However, in our realization, we have introduced a new way to realize ray-shifting lenses. We point out that only a 2D momentum-space distribution of the transmittance and transmissive phases is required to realize the ray-shifting imaging. To introduce such a distribution, it is not necessary to design a 3D metamaterial and consider optical path lengths. Instead, the momentum-space phase modulation required to shift the rays can be induced by the guided resonance supported by the ultrathin 2D PhC slab. We only need to design the dispersion of guided resonances in 2D momentum space. With a relaxed structural requirement, we are able to make the thickness of the resonant layer in

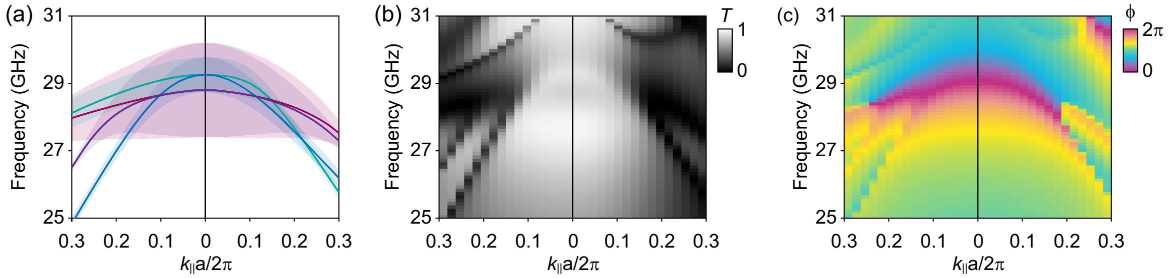

FIG. 4. Simulation results. (a) Eigenfrequency simulation results. The blue and green lines correspond to the transverse-electric-like resonances (even mirror-symmetric), which are degenerate at the Γ point enforced by the C_{6v} symmetry of the structure, while the purple and red lines correspond to the transverse-magnetic-like resonances (odd mirror-symmetric). The shaded areas with the corresponding colors represent the linewidths of the resonances. (b) Simulated transmittance spectra. (c) Simulated transmissive phase spectra.

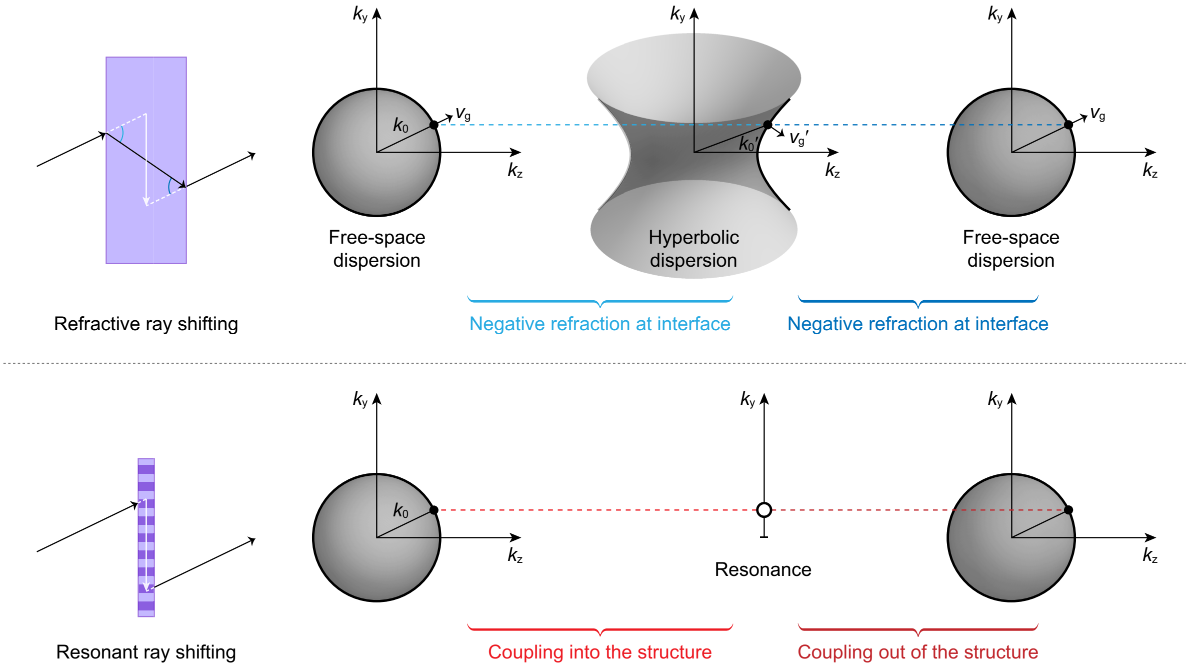

FIG. 5. Difference in the mechanisms of the ray-shifting effect led by negative refraction and by resonances. The momentum-space phase distribution necessary for ray shifts is induced by the optical path lengths in negative refraction slabs. The 3D dispersions of negative refraction slabs have been carefully designed to control the path lengths. On the other hand, the phase modulation is induced by the coupling between guided resonances and free-space plane waves in our realization. Only 2D dispersion engineering is necessary.

our realization only one-tenth of the wavelength, while the entire structure with the cladding layers is only one wavelength thick. Thus, effective medium theories are not applicable to our structure, and no z-direction propagation can be defined for the guided resonances. In other words, there is no "k-surface" spanned in 3D momentum space in our structure as our structure works as an interface rather than a medium.

In summary, we design the transmissive phase and amplitude in 2D momentum space by implementing guided resonances rather than designing the bulk dispersion of a metamaterial in 3D momentum space. Our structure has no effective medium description or "k-surface" spanned in 3D momentum space, and our realization is hence distinct from negative refraction slabs. Reciprocal lenses based on guided resonances are easy to design and can be made ultrathin.

APPENDIX E: EXPERIMENTAL SETUPS

In this appendix, we show the experiment setups. The spectra in Fig. 2(b) are obtained by utilizing an angle-resolved spectra measuring system, as shown in Fig. 6(a). We have two circularly polarized lens antennas connected to a vector network analyzer (VNA, Keysight N5245B) via coaxial cables. One of the antennas acts as the source (transmitter), and the other works as the receiver; the two antennas face each other. The photonic crystal slab sample that functions as the designed reciprocal lens can be mounted on a sample rack with a rotatable stage in the middle of the antennas. Both antennas are arranged far away from the stage; hence, plane-wave incidence can be assumed. We measure the amplitudes and phases of the transmitted waves with and without the sample mounted so that the transmission coefficients can be calculated.

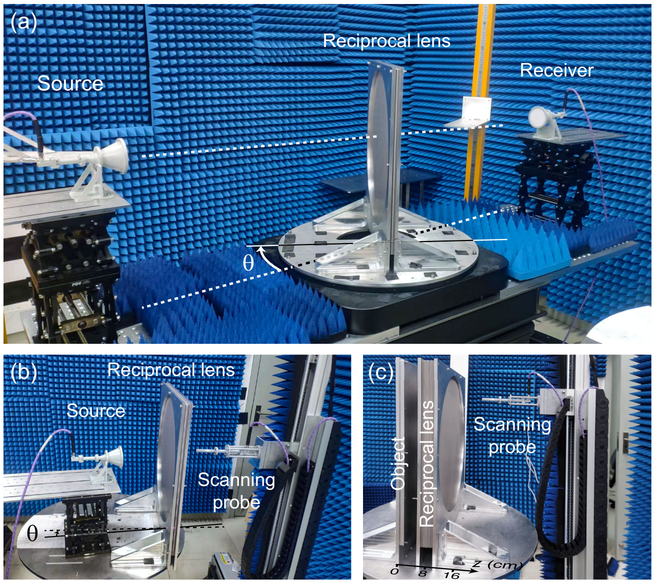

FIG. 6. Experiment setups. (a) Angle-resolved spectra measuring system. (b) Beam-profile measuring system for angle-resolved beam-shift measurements. (c) Imaging testing system.

By scanning the frequency with the VNA (with time grating) and changing the incident elevation angle θ, we are able to obtain the angle-resolved spectra. We can also rotate the sample azimuthally to change the direction measured in wavevector space. A few absorbing layers are attached to the surrounding walls and the table below to reduce the undesired background scattering noise.

On the other hand, the beam-shifting data in Fig. 2(c) are obtained with a beam profile measuring system, which is shown in Fig. 6(b). In this system, the position and the angle of the sample rack are fixed. A lens antenna works as the beam source from which a Gaussian-like beam is emitted. The antenna is placed close to the sample rack this time. The incident elevation angle θ can be changed by rotating the lens antenna. We measure the outgoing field profiles with a scanning probe on the other side of the sample rack. The beam shifts can be obtained by subtracting the positions of beam centroids without the reciprocal lens from the ones with the reciprocal lens.

For the imaging tests, the profile measuring system is slightly modified. As plotted in Fig. 6(c), the horn antenna is now arranged far away to give a plane-wave incidence. A metallic plate with a letter-shaped slot cut, whose position is marked as "$z = 0$," is placed in front of the reciprocal lens, which is located at $z = 3$ cm for the single-layered sample and $z = 8$ cm for the double-layered sample. The slot in the plate is illuminated uniformly by the horn antenna and acts as the object to be imaged. On the other side of the reciprocal lens, the scanning probe captures the transmitted field at a specific z (7.5 cm for the single-layered sample and 16 cm for the double-layered sample).

APPENDIX F: MEASURED BEAM PROFILES IN BEAM-SHIFTING EXPERIMENTS

In the main text, we show the measured shifts of beams with different incident angles given by the reciprocal lens. In Fig. 2, we only plot the centroids of the beams. We plot the measured intensity distributions of the transmitted beams in Fig. 7. Because the input beam is not a perfect Gaussian beam and the output beam is not measured in its transverse plane [see Fig. 6(b)], the positions of the centroids slightly deviate from the positions of the intensity peaks.

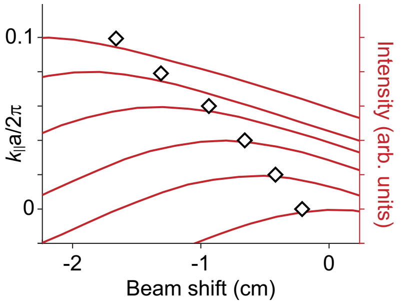

FIG. 7. Intensity distributions of the shifted beams (curves) and their centroids (diamonds). The intensity curves are normalized and shifted in the y axis according to their incident in-plane wave vectors (incident angles) for clarity.

[1] F. A. Jenkins and H. E. White, *Fundamentals of Optics*, 4th ed. (McGraw-Hill Companies, New York, 1976).

[2] M. Born, E. Wolf, A. B. Bhatia, P. C. Clemmow, D. Gabor, A. R. Stokes, A. M. Taylor, P. A. Wayman, and W. L. Wilcock, *Principles of Optics*, 7th ed. (Cambridge University Press, Cambridge, England, 1999).

[3] E. Hecht, *Optics*, 5th ed. (Pearson Education, London, United Kingdom, 2017).

[4] T. Ito and S. Okazaki, *Pushing the Limits of Lithography*, Nature (London) **406**, 1027 (2000).

[5] A. Biswas, I. S. Bayer, A. S. Biris, T. Wang, E. Dervishi, and F. Faupel, *Advances in Top–Down and Bottom–Up Surface Nanofabrication: Techniques, Applications & Future Prospects*, Adv. Colloid Interface Sci. **170**, 2 (2012).

[6] J. J. Hester *et al.*, *Hubble Space Telescope WFPC2 Imaging of M16: Photoevaporation and Emerging Young Stellar Objects*, Astron. J. **111**, 2349 (1996).

[7] R. Nan, D. Li, C. Jin, Q. Wang, L. Zhu, W. Zhu, H. Zhang, Y. Yue, and L. Qian, *The Five-Hundred-Meter Aperture Spherical Radio Telescope (FAST) Project*, Int. J. Mod. Phys. D **20**, 989 (2011).

[8] M. V. Rybin, D. S. Filonov, K. B. Samusev, P. A. Belov, Y. S. Kivshar, and M. F. Limonov, *Phase Diagram for the Transition from Photonic Crystals to Dielectric Metamaterials*, Nat. Commun. **6**, 10102 (2015).

[9] M. Khorasaninejad, W. T. Chen, R. C. Devlin, J. Oh, A. Y. Zhu, and F. Capasso, *Metalenses at Visible Wavelengths: Diffraction-Limited Focusing and Subwavelength Resolution Imaging*, Science **352**, 1190 (2016).

[10] S. Wang, P. C. Wu, V.-C. Su, Y.-C. Lai, M.-K. Chen, H. Y. Kuo, B. H. Chen, Y. H. Chen, T.-T. Huang, J.-H. Wang, R.-M. Lin, C.-H. Kuan, T. Li, Z. Wang, S. Zhu, and D. P. Tsai, *A Broadband Achromatic Metalens in the Visible*, Nat. Nanotechnol. **13**, 227 (2018).

[11] G. Li, *Achromatic Metasurface Lens at Visible Wavelengths*, Sci. Bull. **63**, 333 (2018).

[12] C. Schlickriede, S. S. Kruk, L. Wang, B. Sain, Y. Kivshar, and T. Zentgraf, *Nonlinear Imaging with All-Dielectric Metasurfaces*, Nano Lett. **20**, 4370 (2020).

[13] Y. Fan, M. K. Chen, M. Qiu, R.-J. Lin, Y. Xu, J. Wen, T. Tang, X. Liu, W. Jin, D. P. Tsai, and D. Lei, *Experimental Demonstration of Genetic Algorithm Based Metalens Design for Generating Side-Lobe-Suppressed, Large Depth-of-Focus Light Sheet*, Laser Photonics Rev. **16**, 2100425 (2021).

[14] B. Fu, T. Li, X. Zou, J. Ren, Q. Yuan, S. Wang, X. Cao, Z. Wang, and S. Zhu, *Steerable Chromatic Dispersive Metalenses in Dual Bands*, J. Phys. D **55**, 255105 (2022).

[15] X. Hua, Y. Wang, S. Wang, X. Zou, Y. Zhou, L. Li, F. Yan, X. Cao, S. Xiao, D. P. Tsai, J. Han, Z. Wang, and S. Zhu, *Ultra-Compact Snapshot Spectral Light-Field Imaging*, Nat. Commun. **13**, 2732 (2022).

[16] S.-W. Moon, C. Lee, Y. Yang, J. Kim, T. Badloe, C. Jung, G. Yoon, and J. Rho, *Tutorial on Metalenses for Advanced Flat Optics: Design, Fabrication, and Critical Considerations*, J. Appl. Phys. **131**, 091101 (2022).
[17] C. Xia, E. Bustamante, S. M. Kuebler, N. P. Martinez, R. C. Rumpf, and J. E. Touma, *Binary-Lens-Embedded Photonic Crystals*, Opt. Lett. **47**, 2943 (2022).
[18] N. Yu, P. Genevet, M. A. Kats, F. Aieta, J.-P. Tetienne, F. Capasso, and Z. Gaburro, *Light Propagation with Phase Discontinuities: Generalized Laws of Reflection and Refraction*, Science **334**, 333 (2011).
[19] F. Aieta, P. Genevet, M. A. Kats, N. Yu, R. Blanchard, Z. Gaburro, and F. Capasso, *Aberration-Free Ultrathin Flat Lenses and Axicons at Telecom Wavelengths Based on Plasmonic Metasurfaces*, Nano Lett. **12**, 4932 (2012).
[20] K. Y. Bliokh and A. Aiello, *Goos–Hänchen and Imbert–Fedorov Beam Shifts: An Overview*, J. Opt. **15**, 014001 (2013).
[21] V. G. Veselago, *The Electrodynamics of Substances with Simultaneously Negative Values of ε and μ*, Sov. Phys. Usp. **10**, 509 (1968).
[22] H. Kosaka, T. Kawashima, A. Tomita, M. Notomi, T. Tamamura, T. Sato, and S. Kawakami, *Superprism Phenomena in Photonic Crystals*, Phys. Rev. B **58**, R10096 (1998).
[23] J. B. Pendry, *Negative Refraction Makes a Perfect Lens*, Phys. Rev. Lett. **85**, 3966 (2000).
[24] D. R. Smith, J. B. Pendry, and M. C. K. Wiltshire, *Metamaterials and Negative Refractive Index*, Science **305**, 788 (2004).
[25] N. Fang, H. Lee, C. Sun, and X. Zhang, *Sub-Diffraction-Limited Optical Imaging with a Silver Superlens*, Science **308**, 534 (2005).
[26] G. V. Eleftheriades and K. G. Balmain, *Negative-Refraction Metamaterials* (John Wiley & Sons, New York, 2005).
[27] N. Engheta and R. W. Ziolkowski, *Metamaterials* (John Wiley & Sons, New York, 2006).
[28] Z. Liu, H. Lee, Y. Xiong, C. Sun, and X. Zhang, *Far-Field Optical Hyperlens Magnifying Sub-Diffraction-Limited Objects*, Science **315**, 1686 (2007).
[29] J. Yao, Z. Liu, Y. Liu, Y. Wang, C. Sun, G. Bartal, A. M. Stacy, and X. Zhang, *Optical Negative Refraction in Bulk Metamaterials of Nanowires*, Science **321**, 930 (2008).
[30] J. Valentine, S. Zhang, T. Zentgraf, E. Ulin-Avila, D. A. Genov, G. Bartal, and X. Zhang, *Three-Dimensional Optical Metamaterial with a Negative Refractive Index*, Nature (London) **455**, 376 (2008).
[31] Z. J. Wong, Y. Wang, K. O'Brien, J. Rho, X. Yin, S. Zhang, N. Fang, T.-J. Yen, and X. Zhang, *Optical and Acoustic Metamaterials: Superlens, Negative Refractive Index and Invisibility Cloak*, J. Opt. **19**, 084007 (2017).
[32] D. R. Smith and D. Schurig, *Electromagnetic Wave Propagation in Media with Indefinite Permittivity and Permeability Tensors*, Phys. Rev. Lett. **90**, 077405 (2003).
[33] D. Schurig and D. R. Smith, *Spatial Filtering Using Media with Indefinite Permittivity and Permeability Tensors*, Appl. Phys. Lett. **82**, 2215 (2003).
[34] D. R. Smith, D. Schurig, J. J. Mock, P. Kolinko, and P. Rye, *Partial Focusing of Radiation by a Slab of Indefinite Media*, Appl. Phys. Lett. **84**, 2244 (2004).
[35] J. Elser, R. Wangberg, V. A. Podolskiy, and E. E. Narimanov, *Nanowire Metamaterials with Extreme Optical Anisotropy*, Appl. Phys. Lett. **89**, 261102 (2006).
[36] A. Fang, T. Koschny, and C. M. Soukoulis, *Optical Anisotropic Metamaterials: Negative Refraction and Focusing*, Phys. Rev. B **79**, 245127 (2009).
[37] A. Poddubny, I. Iorsh, P. Belov, and Y. Kivshar, *Hyperbolic Metamaterials*, Nat. Photonics **7**, 948 (2013).
[38] Z. Lu, J. A. Murakowski, C. A. Schuetz, S. Shi, G. J. Schneider, and D. W. Prather, *Three-Dimensional Subwavelength Imaging by a Photonic-Crystal Flat Lens Using Negative Refraction at Microwave Frequencies*, Phys. Rev. Lett. **95**, 153901 (2005).
[39] T. Xu, A. Agrawal, M. Abashin, K. J. Chau, and H. J. Lezec, *All-Angle Negative Refraction and Active Flat Lensing of Ultraviolet Light*, Nature (London) **497**, 470 (2013).
[40] F. Monticone, C. A. Valagiannopoulos, and A. Alu, *Parity-Time Symmetric Nonlocal Metasurfaces: All-Angle Negative Refraction and Volumetric Imaging*, Phys. Rev. X **6**, 041018 (2016).
[41] E. Yablonovitch, *Inhibited Spontaneous Emission in Solid-State Physics and Electronics*, Phys. Rev. Lett. **58**, 2059 (1987).
[42] S. John, *Strong Localization of Photons in Certain Disordered Dielectric Superlattices*, Phys. Rev. Lett. **58**, 2486 (1987).
[43] S. G. Johnson, S. Fan, P. R. Villeneuve, J. D. Joannopoulos, and L. A. Kolodziejski, *Guided Modes in Photonic Crystal Slabs*, Phys. Rev. B **60**, 5751 (1999).
[44] S. Fan and J. D. Joannopoulos, *Analysis of Guided Resonances in Photonic Crystal Slabs*, Phys. Rev. B **65**, 235112 (2002).
[45] C. Guo, H. Wang, and S. Fan, *Squeeze Free Space with Nonlocal Flat Optics*, Optica **7**, 1133 (2020).
[46] C. Guo, M. Xiao, M. Orenstein, and S. Fan, *Structured 3D Linear Space–Time Light Bullets by Nonlocal Nanophotonics*, Light **10**, 160 (2021).
[47] O. Y. Long, C. Guo, W. Jin, and S. Fan, *Polarization-Independent Isotropic Nonlocal Metasurfaces with Wavelength-Controlled Functionality*, Phys. Rev. Appl. **17**, 024029 (2022).
[48] M. Chen, M. Kim, A. M. Wong, and G. V. Eleftheriades, *Huygens' Metasurfaces from Microwaves to Optics: A Review*, Nanophotonics **7**, 1207 (2018).
[49] W. Liu, L. Shi, J. Zi, and C. T. Chan, *Ways to Achieve Efficient Non-Local Vortex Beam Generation*, Nanophotonics **10**, 4297 (2021).
[50] G. V. Eleftheriades, M. Kim, V. G. Ataloglou, and A. H. Dorrah, *Prospects of Huygens' Metasurfaces for Antenna Applications*, Engineering **11**, 21 (2022).
[51] T. J. Davis, F. Eftekhari, D. E. Gómez, and A. Roberts, *Metasurfaces with Asymmetric Optical Transfer Functions for Optical Signal Processing*, Phys. Rev. Lett. **123**, 013901 (2019).
[52] L. Wesemann, J. Rickett, J. Song, J. Lou, E. Hinde, T. J. Davis, and A. Roberts, *Nanophotonics Enhanced Coverslip for Phase Imaging in Biology*, Light **10**, 98 (2021).
[53] L. Wesemann, J. Rickett, T. J. Davis, and A. Roberts, *Real-Time Phase Imaging with an Asymmetric Transfer Function Metasurface*, ACS Photonics **9**, 1803 (2022).

[54] A. Ji, J.-H. Song, Q. Li, F. Xu, C.-T. Tsai, R. C. Tiberio, B. Cui, P. Lalanne, P. G. Kik, D. A. B. Miller, and M. L. Brongersma, *Quantitative Phase Contrast Imaging with a Nonlocal Angle-Selective Metasurface*, Nat. Commun. **13**, 7848 (2022).

[55] A. Cordaro, H. Kwon, D. Sounas, A. F. Koenderink, A. Alù, and A. Polman, *High-Index Dielectric Metasurfaces Performing Mathematical Operations*, Nano Lett. **19**, 8418 (2019).

[56] Y. Zhou, H. Zheng, I. I. Kravchenko, and J. Valentine, *Flat Optics for Image Differentiation*, Nat. Photonics **14**, 316 (2020).

[57] T. Zhu, C. Guo, J. Huang, H. Wang, M. Orenstein, Z. Ruan, and S. Fan, *Publisher Correction: Topological Optical Differentiator*, Nat. Commun. **12**, 680 (2021).

[58] S. Fan, W. Suh, and J. D. Joannopoulos, *Temporal Coupled-Mode Theory for the Fano Resonance in Optical Resonators*, J. Opt. Soc. Am. A **20**, 569 (2003).

[59] K. Sakoda, *Optical Properties of Photonic Crystals*, Vol. 80 (Springer, Berlin, Heidelberg, 2005).

[60] B. Zhen, C. W. Hsu, L. Lu, A. D. Stone, and M. Soljačić, *Topological Nature of Optical Bound States in the Continuum*, Phys. Rev. Lett. **113**, 257401 (2014).